



Tube-based robust model predictive control for fault tolerance[☆]

Elyse Hill^a, Andrew Newton^b, S. Andrew Gadsden^{b,*}, Mohammad Biglarbegian^c

^a NASA Glenn Research Center, Cleveland, 44135, OH, USA

^b Department of Mechanical Engineering, McMaster University, Hamilton, L8S 4L8, Ontario, Canada

^c Department of Mechanical and Aerospace Engineering, Carleton University, Ottawa, K1S 5B6, Ontario, Canada

ARTICLE INFO

Keywords:

Nonlinear model predictive control
Robust NMPC
Fault tolerant control
Sliding mode control (SMC)
Uncertain systems

ABSTRACT

This paper presents a robust, fault tolerant, tube-based nonlinear model predictive controller for systems with additive external disturbances and actuator faults. The design exploits the sliding mode control design embedded in the auxiliary controller to create a lumped disturbance upper bound that represents the worst-case contribution of both faults and disturbances. In this way, the proposed design is shown to maintain robust control invariance in the presence of both forms of uncertainty. The design is expanded in two ways which utilize a double boundary layer for the sliding surface to create a blended tube design, permitting the control to take advantage of disturbance-based and lumped disturbance-based tubes. The proposed designs are implemented on the attitude control of a nanosatellite system in both simulation and experimentation, where performance is evaluated with average root mean square values on the attitude and input variables. Simulation results reveal the proposed fault-tolerant technique maintains robust control invariance in the presence of faults, unlike its nominal counterpart. Additionally, use of a double boundary layer and blended tube significantly improved tracking performance at little increase in control effort while still maintaining robust control invariance. Experimental results establish the validity of the fault-tolerant technique in practice on a model nanosatellite.

1. Introduction

Real world systems are plagued by uncertainty in the form of disturbances, noise, or faults. Although many controllers possess inherent robustness to disturbances and noise, faults can cause serious degradation in controller performance and lead to instability. Thus, fault tolerant control (FTC) schemes are of interest, designed with the goal to mitigate or correct the effect of faulty conditions, such as sensor or actuator failures [1]. In general, FTC methods can be distinguished as passive or active [2]. The passive approach lends itself to robust control techniques and focuses on resilience against the worst possible failure while the active approach focuses on diagnosis and adjustment to faults, inviting more adaptive control approaches [3–9].

In recent years, MPC has found increasing use in FTC schemes [10–12]. Specifically, robust MPC approaches, i.e. min–max or tube-based MPC, have been applied actively [13–19] and passively [20–22]. Though effective, the active designs are inherently suboptimal due to the decoupling necessary between fault detection, isolation, and recovery architectures in the controller. Additionally, these designs can be complex to implement due to the need to update system parameters or

change controller structure. Indeed, although potentially conservative, passive FTC's "one-size-fits-all" approach is easy to implement. Because it is designed on the worst case scenario for a system, a passive scheme requires no knowledge of fault activation or of multiple models to maintain system performance. This convenience prompts development of passive FTC schemes employing MPC, such as the works [20–22].

Ref. [20] uses an extended state-space model coupling the states and output tracking error to mitigate uncertainty in industrial processes. In a similar vein, [21] built upon these results by introducing H_∞ performance indexing to increase the robustness of the design proposed by [20] for interval time-varying delays and partial actuator failure. Recently, [22] has used a similar approach for time delay systems, combining the extended state-space model with a parameter dependent Lyapunov-Krasovskii functional to mitigate uncertainties caused by actuator faults, time delay, and external disturbances. However, these studies were limited to linear systems and were exclusive to min–max robust MPC approaches, which is more computationally complex than tube-based MPC. To the authors' best knowledge, only the work of [23] has considered FTC for tube-based MPC on a nonlinear system. Unfortunately, this approach is active rather than passive, using multiple fault

[☆] This paper was recommended for publication by Associate Editor Roger Dixon.

* Corresponding author.

E-mail addresses: elyse.d.hill@nasa.gov (E. Hill), newtoa4@mcmaster.ca (A. Newton), gadsden@mcmaster.ca (S.A. Gadsden), mohammad.biglarbegian@carleton.ca (M. Biglarbegian).

<https://doi.org/10.1016/j.mechatronics.2023.103051>

Received 19 February 2022; Received in revised form 20 April 2023; Accepted 12 August 2023

Available online 19 September 2023

0957-4158/© 2023 Elsevier Ltd. All rights reserved.

models in its design to steer the system trajectories from a nominal to a safety set in the event of a fault. Thus, there is a current gap in the literature surrounding passive FTC methods with tube-based MPC for nonlinear systems that should be addressed.

In this paper, we propose a passive fault tolerant tube-based MPC for nonlinear systems with additive external disturbances and actuator faults. This is accomplished using a tube-based controller that cascades an NMPC and a model predictive sliding mode controller (MPSMC). The primary contribution lies in exploiting the tube size design with sliding mode control, resulting in three main outcomes: (1) inclusion of a lumped disturbance bound that accounts for disturbances and faults; (2) design of a double boundary layer to mitigate response to faults; and (3) use of a blended tube design to reduce conservatism. The subsequent design relies only on one system model and requires no change to its nominal online constraint tightening scheme, resulting in minimal increase to conceptual complexity. The proposed method is implemented in simulation and in experimentation on a nonlinear nanosatellite system perturbed by disturbances and actuator failures. Controller performance is evaluated using root mean squared values on the control effort and the states.

The remainder of this paper is organized as follows: Section 2 overviews the problem statement, followed by a description of the underlying tube-based NMPC strategy in Section 3. The proposed fault tolerant controller is detailed in Section 4 and Section 5 describes the mathematical model for validation. Section 6 provides simulation and experimental results and discussion, and the paper is concluded in Section 7.

2. Problem setup

Consider the following nonlinear, feedback linearizable, control affine dynamic system:

$$\dot{x}(t) = f(x(t)) + bu(t) + w(t) \quad (1)$$

where $x(t) \in \mathbb{R}^n$ is the system state, $u(t) \in \mathbb{R}^r$ is the system input, $w(t) \in \mathbb{R}^n$ is an external disturbance, $f(\cdot)$ is the system dynamics, and $b \in \mathbb{R}^{n \times r}$ is the input matrix. The solution at time t_0 to (1) for initial condition $x(t_0)$ and piecewise continuous control $u(\cdot) \in \mathcal{L}([t_0, t], \mathbb{R}^r)$ is denoted as $x(\tau; x(t_0), u(\cdot), w(\cdot))$, $\tau \in [t_0, t]$. Here, $\mathcal{L}([a, b], \mathbb{R})$ represents the Lebesgue measurable and essentially bounded functions mapping $u : [a, b] \rightarrow \mathbb{R}$. The system (1) is subject to the constraints $x \in \mathcal{X}$, $u \in \mathcal{U}$, and $w \in \mathcal{W}$, where the constraint sets $\mathcal{X} = \{x \in \mathbb{R}^n | L_x x \leq B_x\}$ and $\mathcal{U} = \{u \in \mathbb{R}^r | L_u u \leq B_u\}$ are convex, closed, and bounded, containing the origin in their interior, and L_x , L_u , B_x , B_u are user determined constants. Further, the external disturbance is bounded to the set $w \in \mathcal{W} := \{w \in \mathbb{R}^n : \|w\| \leq W\}$, where $\|\cdot\|$ denotes the Euclidean norm, W is the upper bound of the disturbance, and \mathcal{W} is closed and bounded, containing the origin in its interior. Let (1) be affected by an actuator fault yielding:

$$\dot{x}(t) = f(x(t)) + b(\mathbb{I}_r - a)u(t) + w(t) \quad (2)$$

where \mathbb{I}_r is an $r \times r$ identity matrix and a is an $r \times r$ diagonal matrix with elements α_i , $i = 1 \dots r$ that indicate actuator effectiveness and are bounded as $0 \leq \alpha_i \leq \bar{\alpha}_i \leq 1$ where $\alpha_i = 0$ represents nominal operating condition, $\bar{\alpha}_i$ represents the upper bound of an actuator's effectiveness, and $\alpha_i = 1$ represents complete actuator failure. Defining $u_F(t) = -au(t)$, the faulty system can now be described as:

$$\dot{x}(t) = f(x(t)) + bu(t) + bu_F(t) + w(t) \quad (3)$$

Considering the fault and the disturbance as a lumped disturbance term produces:

$$\dot{x}(t) = f(x(t)) + bu(t) + w_L(t) \quad (4)$$

where $w_L(t) = bu_F(t) + w(t)$ with $w_L(t) \in \mathbb{R}^n$ now represents the sum of actuator failures and external disturbances. The control goal is to stabilize the closed-loop of (4) subject to state and input constraints and

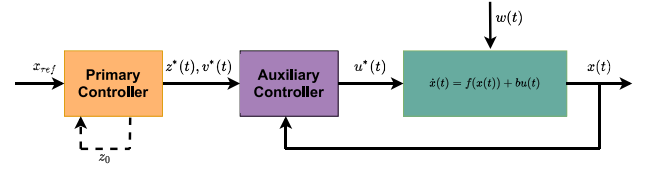


Fig. 1. Block diagram of controller architecture.

any possible uncertainty upper bounded by $W_L = W + \bar{\alpha}B_u$, which now represents both external disturbances and additive faults and where $\bar{\alpha}B_u$ is the upper bound of the actuator faults. In this paper, this goal will be addressed using tube-based robust MPC, which partners the optimal control input $v^*(t)$ from a primary controller and the input κ from an auxiliary controller to control (4). Specifically, we focus on modifying the tube-based method with the lumped disturbance bound such that the true system trajectory $x(t)$ remains in a robust control invariant (RCI) set around an optimal nominal trajectory $z^*(t)$.

Definition 1 (Robust Control Invariant Set). Let $e(t) := x(t) - z^*(t)$. A set $S \subseteq \mathcal{X}$ is a RCI set if there exists a control $\kappa \in \mathcal{U}$ such that if $e(t_0) \in S$, then for all allowable $w(t) \in \mathcal{W}$, it holds that $e(t) \in S \quad \forall t \geq t_0$.

Thus, fault tolerance in the scope of this work will refer to the ability of the tube-based RMPC to maintain RCI in the presence of both forms of uncertainty, additive actuator faults and external disturbances.

Remark 1. The term $\bar{\alpha}$ is included as the upper bound of the actuator effectiveness for two reasons: (1) to allow the user to define an admissible region of the actuator faults and (2) to avoid the underactuated scenario of $\bar{\alpha} = \mathbb{I}_r$, which is not under examination in this study. Similar to selecting an appropriate disturbance upper bound W , $\bar{\alpha}$ can be selected based on the **expected** amount of potential actuator degradation. This is not an unreasonable assumption, as typical methods of failure and their effects are known for physical systems.

Remark 2. For purposes of simplicity, subsequent analysis will consider that (1) and its iterations can be defined by a double integrator model with a single input (i.e. $n = 2, r = 1$). However, all analysis can be extended to multi-input, feedback linearizable systems, including square systems.

3. Controller design

This section presents the development of the tube-based robust MPC controller formed using a model predictive sliding mode controller, termed NMPC-MPSMC. Introduced in [24], to account solely for bounded disturbances, the architecture features a primary controller cascaded with an auxiliary controller, as shown in Fig. 1. In this scheme, a sampled-data NMPC is the primary controller and a sampled-data MPSMC is the auxiliary controller. Both controllers are designed based on an undisturbed system model ($w_L = 0$) with assumed system dynamics \hat{f} described as:

$$\dot{x}(t) = \hat{f}(x(t)) + \hat{b}u(t) \quad (5)$$

For the remainder of the analysis, we assume no uncertainty exists in the input channel such that $\hat{b} = b$.

3.1. Primary controller

The primary controller is designed to control (5) with nominal state $z(t) \in \mathcal{Z} \subset \mathcal{X}$ and nominal input $v(t) \in \mathcal{V} \subset \mathcal{U}$, where \mathcal{Z}, \mathcal{V} are tightened state and input constraints. The optimal control problem solved at

sampling instant $t_k = kT_s$, where $k \in \mathbb{N}$ and constant sampling time $T_s \in \mathbb{R}_{\geq 0}$, is:

$$v(\cdot) \in \mathcal{S}([t_k, t_k + T], \mathbb{R}) \quad J_{T, \text{nom}} \quad (6a)$$

subject to

$$\dot{z}(\tau) = \hat{f}(z(\tau)) + bv(\tau), \quad (6b)$$

$$z(t_k) = z_0, \quad (6c)$$

$$z(\tau) \in \mathcal{Z}, \quad v(\tau) \in \mathcal{V}, \quad (6d)$$

$$z(t_k + T) \in \mathcal{Z}_f, \quad (6e)$$

$$\tau \in [t_k, t_k + T]$$

where $z(t_k)$ is the initial state, z_0 is the solution to (5) with the optimal input determined by (6) at the previous sampling instant, T is the time horizon, $\mathcal{Z}_f \subset \mathcal{X}$ is a tightened terminal constraint set, and the open-loop cost function is:

$$J_{T, \text{nom}} = \int_{t_k}^{t_k + T} l_{\text{nom}}(z(\tau), v(\tau)) d\tau + V_{f, \text{nom}}(z(t_k + T)) \quad (7)$$

where the cost functions are defined as quadratic stage cost $l_{\text{nom}}(z, v) = \|z - x_{\text{ref}}\|_Q^2 + \|v\|_R^2$ and quadratic terminal cost $V_{f, \text{nom}}(z) = \|z - x_{\text{ref}}\|_P^2$ which are weighted by positive semi-definite matrix Q and positive definite matrices R and P . Here, $\|x\|_H^2$ denotes a norm weighted by a symmetric matrix H . The subscript $(\cdot)_{\text{nom}}$ indicates the function belongs to the primary controller and x_{ref} is the reference trajectory that can be defined as a static set-point or as a time-varying signal. Note at $t = t_0$, initial condition z_0 is initialized as $z_0 = x_{\text{ref}}(t_0)$. The outputs to (6) are an optimal open-loop input sequence along the time horizon $v^*(\cdot; z(t_k))$ and its associated optimal state trajectory $z^*(\cdot; z(t_k), v^*(\cdot; z(t_k)))$, where $(\cdot)^*$ denotes the optimal solution. Only the portion of the input sequence pertaining to $t \in [t_k, t_{k+1})$ is applied to the system (5) until the next sampling instant t_{k+1} .

3.2. Auxiliary controller

The auxiliary controller is used to counteract the effects of the disturbance w by maintaining the true system trajectory x close to the nominal trajectory z . The MPSMC accomplishes this by minimizing the deviation from zero of a sliding variable designed on the error between the optimal nominal trajectory and a predicted, undisturbed system trajectory initialized with the current state of the system. Specifically, the sliding variable is designed as:

$$s = \dot{e}_t(t) + \lambda e_t(t) \quad (8)$$

where $e_t(t) = \check{x}(t) - z^*(t; z(t_k), v^*(t; z(t_k)))$, $t \in [t_k, t_k + T]$, $\lambda > 0$ is a scalar gain, and the superscript (\cdot) indicates variables internal to the auxiliary optimal control problem. Then, the auxiliary control problem can be defined by:

$$\check{u}(\cdot) \in \mathcal{S}([t_k, t_k + T], \mathbb{R}) \quad J_{T, \text{aux}} \quad (9a)$$

subject to

$$\dot{\check{x}}(\tau) = \hat{f}(\check{x}(\tau)) + b(\check{u}(\tau) + b^{-1} \bar{K}(\check{x}(\tau)) \text{sat}(\check{s}(\tau), \check{\Phi}(\tau))) - \ddot{x}_d(\tau) + \lambda \dot{e}_t(\tau), \quad (9b)$$

$$\dot{\check{x}}(\tau) = \hat{f}(\check{x}(\tau)) + b\check{u}(\tau), \quad (9c)$$

$$\dot{\check{\Phi}}(\tau) = -\lambda' \check{\Phi}(\tau) + F(x_d(\tau)) + W + \eta, \quad (9d)$$

$$\dot{\check{S}}(\tau) = A\check{S}(\tau) + B\check{\Phi}(\tau), \quad (9e)$$

$$\check{x}(t_k) = x(t_k), \quad \check{s}(t_k) = s(t_k), \quad (9f)$$

$$\check{\Phi}(t_k) = \Phi_0, \quad \check{S}(t_k) = |e(t_k)|, \quad (9g)$$

$$\check{x}(\tau) \in \mathcal{X}, \quad \check{u}(\tau) \in \mathcal{U}, \quad (9h)$$

$$\check{x}(t_k + T) \in \mathcal{X}_f, \quad (9i)$$

$$\tau \in [t_k, t_k + T]$$

where λ' is the control bandwidth, $\eta > 0$ is a design parameter satisfying the sliding condition, and $\bar{K}(x)$ is a gain determined by:

$$\begin{aligned} \bar{K}(x) &= F(x) + W + \eta - \dot{\Phi} \\ &= F(x) - F(x_d) + \lambda' \Phi \end{aligned} \quad (10)$$

where Φ is the boundary layer thickness and the nonlinear dynamics are bound by an assumed model error function $F(x) \geq |f(x) - \hat{f}(x)|$. Use of $F(x)$ permits system uncertainty to be captured and is justifiable because in practice, users tend to know ranges of parameter deviations for dynamic systems. Eq. (9) is subjected to sliding mode dynamics (9b), system dynamics (9c), boundary layer thickness dynamics (9d), tube dynamics (9e), initial conditions on the system, sliding variable, boundary layer, and tube size (9f)–(9g), and state and input constraints (9h)–(9i). In (9), $x_d(\tau)$ and its derivatives are the associated optimal nominal state trajectory from (6) and $\Phi_0 = \dot{\Phi}^*(t_{k+1}; s(t_k), \check{u}^*(\cdot))$ from the previous sampling instant. Eq. (9d) describes the boundary layer thickness Φ as a function of the maximum disturbance bound W , sliding parameter η , and the model error function $F(x)$. Eq. (9e) describes the tube geometry, denoted as S , that bounds the error between the true system trajectory and the optimal nominal trajectory defined as $e(t) := x(t) - z^*(t; z(t_k), v^*(t; z(t_k)))$, $t \in [t_k, t_{k+1})$, where $A = -\lambda$ and $B = \mathbb{I}_r$, such that all realizations of x are RCI with respect to z^* . The open-loop cost function of (9) is:

$$J_{T, \text{aux}} = \int_{t_k}^{t_k + T} l_{\text{aux}}(\check{s}(\tau), \check{u}(\tau)) d\tau + V_{f, \text{aux}}(\check{s}(t_k + T)) \quad (11)$$

where the cost functions are defined as quadratic stage cost $l_{\text{aux}}(s, u) = \|s\|_Q^2 + \|u\|_R^2$, quadratic terminal cost $V_{f, \text{aux}}(s) = \|s\|_P^2$, Q' is a positive semi-definite matrix, R' , P' are positive definite matrices, and the subscript $(\cdot)_{\text{aux}}$ indicates the function belongs to the auxiliary controller.

The optimal open-loop control input $\check{u}^*(\cdot; s(t_k))$ is the solution to (9) which is applied to (1) until the next sampling instant t_{k+1} . Note from (9b) this value represents the total control input based on a manipulation of the sliding mode derivation as detailed in [24]. The auxiliary controller also produces associated optimal trajectories for the sliding surface, state trajectories, boundary layer thickness, and tube size. The tube size is used to determine the tightened constraint sets as:

$$\mathcal{Z} = \{z \in \mathbb{R}^n : L_x z \leq B_x - L_x S_{\text{opt}}\} \quad (12)$$

$$\mathcal{V} = \{v \in \mathbb{R}^r : L_u v \leq B_u - L_u b^{-1} \bar{K}_{\text{max}}(x(t))\} \quad (13)$$

where $S_{\text{opt}} = \check{S}^*(t; s(t_k), \check{u}^*(t; s(t_k)))$, $t \in [t_k, t_{k+1})$ is the optimized tube size and gain $\bar{K}_{\text{max}}(x(t))$ is defined by

$$\bar{K}_{\text{max}}(x(t)) = \max\{\bar{K}(x_{lb}), \bar{K}(x_{ub})\}, \quad t \in [t_k, t_{k+1}) \quad (14)$$

where $x_{lb} = z^*(t; z(t_k), v^*(t; z(t_k))) - S_{\text{opt}}(t)$, $x_{ub} = z^*(t; z(t_k), v^*(t; z(t_k))) + S_{\text{opt}}(t)$, and $\max\{\cdot\}$ is the element-by-element maximum.

Feasibility and convergence of the abovementioned control design has been proven input-to-state stable in [24], where input-to-state stability is justifiable as a tool for analysis based on the results in [25]. Terminal ingredients can be determined through the design of the terminal cost function using methods outlined in [26,27]. However, for simplicity, in this paper terminal ingredients for the primary and auxiliary controllers have been selected such that the nominal terminal constraint set is $\mathcal{Z}_f = \{z_e\}$, where z_e represents a user-defined set of equilibrium states specific to the system dynamics; and such that the auxiliary terminal constraint set is $\mathcal{X}_f = \{x_e\}$, where $x_e = z^*(t_k + T; z(t_k), v^*(t_{k+N-1}; z(t_k)))$ where $N = \frac{T}{T_s}$, a value representing the time horizon in iterative steps.

4. Tube-based MPC with fault tolerant MPSMC

In this section, it will be shown that by introducing the lumped uncertainty bound W_L into the design of the MPSMC, a tube-based controller can be designed that simultaneously considers the effect of actuator faults and external disturbances and maintains robust control invariance of the tube design. Substituting W_L for W in (9d) results in a boundary layer Φ that accounts for external disturbances *and* faults:

$$\dot{\Phi} = -\lambda' \Phi + F(x_d) + W_L + \eta \quad (15)$$

Eq. (15) enlarges the tube size and discontinuous gain value by using W_L as opposed to W , allowing both to mitigate the effect of actuator faults on the system. As a robust technique, this solution is overly conservative, as it considers that actuator faults are active at all times. Further, due to the enlarged tube size, evolutions of the system trajectories may fall in a wider band around the nominal trajectory than if a narrower tube size is employed. Ideally, when no faults exist, the spread of system trajectories around the nominal trajectory for either tube designed on W_L or W should be the same width. To accomplish this, a minor augmentation is proposed in the discontinuous term $\bar{K}(x)\text{sat}(\cdot)$ of (9b) where the saturation function is now:

$$\text{sat}(s, \Phi_W, \Phi_{W_L}) = \begin{cases} \text{sign}(s), & |s| > \Phi_{W_L} \\ \frac{s}{\Phi_{W_L}} + \xi \text{sign}(s), & \Phi_{W_L} \geq |s| > \Phi_W \\ \frac{s}{\Phi_{W_L}} + \xi \frac{s}{\Phi_W}, & \Phi_W \geq |s| \end{cases} \quad (16)$$

where Φ_W defined by (9d) and Φ_{W_L} defined by (15) can be considered as inner and outer boundary layers such that $\Phi_{W_L} > \Phi_W > 0$, and ξ is an $r \times r$ positive, diagonal matrix with elements bounded as $0 \leq \xi_i \leq 1, i = 1 \dots r$. This value can be considered as a gain that determines how aggressively the input will behave to approach Φ_W and mitigate the spread of trajectories. At $\xi_i = 1$ the saturation function fully incorporates Φ_W to mitigate trajectory spread while at $\xi_i = 0$ Φ_W is disregarded, returning the saturation function to its traditional definition with boundary layer Φ_{W_L} . Further, it is possible to use ξ to reduce the conservativeness of $\bar{K}(x)$ and define a more accurate tube size through the following changes to (10) and (9e):

$$\bar{K}(x) = F(x) - F(x_d) + \lambda'[(\mathbb{I}_r - \xi)\Phi_{W_L} + \xi\Phi_W] \quad (17)$$

$$\dot{S}_0 = AS_0 + B[(\mathbb{I}_r - \xi)\Phi_{W_L} + \xi\Phi_W] \quad (18)$$

where now the gain and tube can use a linear combination of both the inner and outer boundary layer sizes to determine a less conservative gain and a tighter tube size.

The values of ξ are user determined, and should be selected to limit trajectory spread around the nominal trajectory. Introducing ξ accomplishes this by bringing (17) closer in value to (10). This technique can be taken further by changing ξ from a static to dynamic variable and introducing it to the optimal control problem (9) by adding:

$$\dot{\xi}(t) = v(t) \quad (19)$$

where v is an artificial control input used to smoothen the optimization of ξ . Thus, the fault tolerant MPSMC, termed FT-MPSMC, can be described by the following optimization problem:

$$\min_{\check{u}(\cdot), \check{v}(\cdot) \in \mathcal{L}([t_k, t_k+T], \mathbb{R}^r)} J_{T,\text{aux}} \quad (20a)$$

subject to

$$\begin{aligned} \dot{\check{x}}(\tau) &= \hat{f}(\check{x}(\tau)) - \check{x}_d(\tau) + \lambda \check{e}_t(\tau) \\ &+ b^{-1} \bar{K}(\check{x}(\tau)) \text{sat}(\check{s}(\tau), \check{\Phi}_W(\tau), \check{\Phi}_{W_L}(\tau)), \end{aligned} \quad (20b)$$

$$\dot{\check{x}}(\tau) = \hat{f}(\check{x}(\tau)) + b\check{u}(\tau), \quad \dot{\xi}(\tau) = v(\tau), \quad (20c)$$

$$\dot{\check{\Phi}}_W(\tau) = -\lambda' \check{\Phi}_W(\tau) + F(x_d(\tau)) + W + \eta, \quad (20d)$$

$$\dot{\check{\Phi}}_{W_L}(\tau) = -\lambda' \check{\Phi}_{W_L}(\tau) + F(x_d(\tau)) + W_L + \eta, \quad (20e)$$

$$\dot{S}(\tau) = AS(\tau) + B[(\mathbb{I}_r - \xi(\tau))\check{\Phi}_{W_L}(\tau) + \xi(\tau)\check{\Phi}_W(\tau)], \quad (20f)$$

$$\check{x}(t_k) = x(t_k), \quad \check{s}(t_k) = s(t_k), \quad (20g)$$

$$\check{\Phi}_W(t_k) = \Phi_{W,0}, \quad \check{\Phi}_{W_L}(t_k) = \Phi_{W_L,0}, \quad (20h)$$

$$\check{S}(t_k) = |e(t_k)|, \quad \check{\xi}(t_k) = \xi_0, \quad (20i)$$

$$\check{x}(\tau) \in \mathcal{X}, \quad \check{\xi}(\tau) \in \Xi, \quad (20j)$$

$$\check{u}(t) \in \mathcal{U}, \quad \check{v}(t) \in \mathcal{Y}, \quad (20k)$$

$$\check{x}(t_k + T) \in \mathcal{X}_f, \quad (20l)$$

$$\tau \in [t_k, t_k + T]$$

where $\bar{K}(x)$ is defined by (17) and the open-loop cost function is now:

$$\begin{aligned} J_{T,\text{aux}} &= \int_{t_k}^{t_k+T} l_{\text{aux}}(\check{s}(\tau), \check{\xi}(\tau), \check{u}(\tau), \check{v}(\tau)) d\tau \\ &+ V_{f,\text{aux}}(\check{s}(t_k + T)) \end{aligned} \quad (21)$$

where the terminal cost is unchanged from (11) and the stage cost is now defined as $l_{\text{aux}}(s, \xi, u, v) = \|s\|_{Q'}^2 + \|u\|_{R'}^2 + \|\mathbb{I}_r - \xi\|_{R''}^2$ and R'' is positive semi-definite. The gain ξ is penalized as the deviation from identity to indicate that (20) should attempt to maintain the disturbance-based tube of (9e) but expand the tube size by transitioning to lumped disturbance-based tube of (18) as necessary. Based on (17), this also adjusts the gain necessary to push the sliding trajectory towards the more heavily weighted boundary layer.

The optimal open-loop control input solution $\check{u}^*(\cdot; s(t_k))$ to (20) is applied to (4) until the next sampling instant t_{k+1} , producing the closed-loop system:

$$\dot{x}(t) = f(x(t)) + bu(t) + w_L(t),$$

$$u(t) = \check{u}^*(\cdot; s(t_k)), t \in [t_k, t_{k+1}] \quad (22)$$

The fault-tolerant MPSMC presented in this section leverages boundary layer sliding mode control design to account for uncertainty (i.e. additive, bounded external disturbances and actuator faults) in a simple and additive manner. The scheme offers a wide degree of freedom, capable of three different implementations: (i) replacing Φ_W with Φ_{W_L} in (9); (ii) implementing (20) without a dynamic internal gain, eliminating (19) and its related equations from the optimization; or (iii) with a dynamic internal gain and resulting optimization problem (20). Additionally, due to the design of (16), the original constraint tightening scheme described in Section 3.2 remains unchanged when implementing (20). Further, the stability results of NMPC-MPSMC hold for FT-NMPC-MPSMC and its derivations as the convergence properties and recursive feasibility of the controller architectures are identical, unaffected by the change in cost function from (11) to (21). Though intricate, the complexity of (20) can be altered depending on implementation (i), (ii), or (iii). Studies on the computational complexity of the design are left as a subject of future work. For the remainder of this paper, the total control produced by cascading (6) and (20) is termed FT-NMPC-MPSMC. To distinguish between the abovementioned forms, FT-NMPC-MPSMC refers to (i), FT-NMPC-MPSMC_ξ refers to (ii), and FT-NMPC-MPSMC_{ξ̄} refers to (iii).

5. Application of developed controller

The proposed fault tolerant tube controller is verified on a nonlinear nanosatellite system actuated with reaction wheels. Reaction wheel failure is common and can lead to degradation in spacecraft pointing accuracy, thus presenting an ideal scenario on which to verify the proposed method. In this paper, we examine an overactuated nanosatellite equipped with four reaction wheels where multiple wheel failures can occur simultaneously.

5.1. Satellite kinematics and dynamics

The attitude of a satellite can be represented by the quaternion $q = [q_1 \ q_2 \ q_3 \ q_4]^T$, composed of vector component $q_{1:3}$ and scalar component q_4 . The quaternion satisfies a norm constraint $\|q\| = 1$ and is used to parameterize the attitude to avoid singularities resulting from Euler angle notation. The kinematic and dynamic equations of a rigid body spacecraft with reaction wheels in the presence of external disturbances and actuator faults (omitting time argument) are:

$$\dot{q} = \frac{1}{2} \Omega(\omega_b) q \quad (23a)$$

$$\dot{\omega}_b = I_b^{-1} [\tau_{ext} - [\omega_b \times] (I_b \omega_b + \mathcal{W} h_w^W) - \mathcal{W} (h_w^W - \alpha h_w^W)] \quad (23b)$$

where $\omega_b = [\omega_x \ \omega_y \ \omega_z]^T$ is the angular velocity of the satellite expressed in the body frame and $I_b \in \mathbb{R}^{3 \times 3}$ is the unknown mass moment of inertia of the satellite body expressed in the body frame. The reaction wheel angular momentum h_w^W is expressed in the wheel frame, indicated by the W superscript, and \dot{h}_w^W is the reaction wheel torque coordinated in the wheel frame. \mathcal{W} is the reaction wheel configuration matrix which maps the wheel torques into the body frame. $\tau_{ext} = [\tau_{ext,x} \ \tau_{ext,y} \ \tau_{ext,z}]^T$ is an external disturbance, and the skew-symmetric matrix $[\omega_b \times]$ and operation $\Omega(\omega_b)$ are

$$\Omega(\omega_b) = \begin{bmatrix} -[\omega_b \times] & \omega_b \\ -\omega_b^T & 0 \end{bmatrix} \quad (24)$$

$$[\omega_b \times] = \begin{bmatrix} 0 & -\omega_z & \omega_y \\ \omega_z & 0 & -\omega_x \\ -\omega_y & \omega_x & 0 \end{bmatrix} \quad (25)$$

For redundancy, satellites are often equipped with more than three reaction wheels. The configuration matrix, \mathcal{W} , maps the resulting wheel torques from the wheel coordinate frame W into the spacecraft body coordinate frame B as:

$$\dot{h}_w^B = \mathcal{W} \dot{h}_w^W \quad (26)$$

This paper considers a pyramidal configuration of the reaction wheel assembly. In this layout, the wheels are skewed by an angle β_1 from each primary axis, and then skewed further by an angle β_2 from the satellite body frame, resulting in the distribution matrix:

$$\mathcal{W} = \begin{bmatrix} c(\beta_1)s(\beta_2) & -c(\beta_1)s(\beta_2) & -c(\beta_1)s(\beta_2) & c(\beta_1)s(\beta_2) \\ -c(\beta_1)c(\beta_2) & -c(\beta_1)c(\beta_2) & c(\beta_1)c(\beta_2) & c(\beta_1)c(\beta_2) \\ s(\beta_1) & s(\beta_1) & s(\beta_1) & s(\beta_1) \end{bmatrix} \quad (27)$$

where $c(\cdot) = \cos(\cdot)$ and $s(\cdot) = \sin(\cdot)$. To introduce actuator faults, the parameter α is applied directly to the reaction wheels, rather than the body equivalent torque. The upper bound of actuator effectiveness can be found by converting α to its equivalent in the body frame. Two methods of failure are explored in this paper: a float failure, represented by $\alpha_i = 1, i = 1 \dots 4$ and resulting in zero actuation, and a loss of efficiency failure, represented by $0 < \alpha_i < 1$ and resulting in actuator degradation by a finite percentage over time. Based on (23) and (26) the system's states are defined as $x = [q \ \omega_b]^T$ and the control input is defined as $u = [-\dot{h}_w^B]^T$. The sliding surface for (23) is defined by:

$$s = \omega_e + \lambda q_{e,1:3} \quad (28)$$

where the state errors are:

$$q_e = q \otimes q_d^{-1} \quad (29)$$

$$\omega_e = \omega_b - \omega_d \quad (30)$$

where q is the measured quaternion, q_d is the desired quaternion, ω_b is the measured angular velocity of the satellite body, ω_d is the desired angular velocity of the satellite body, and the operator $q \otimes$ represents:

$$q \otimes = \begin{bmatrix} q_4 \mathbb{I}_3 - [q_{1:3} \times] & q_{1:3} \\ -q_{1:3}^T & q_4 \end{bmatrix} \quad (31)$$

where $[q_{1:3} \times]$ is identical to (25) using the quaternion vector components, and \mathbb{I}_3 is the 3×3 identity matrix. The model error function is defined as:

$$F(\cdot) = \left[\tilde{I}_b^{-1} [-[\omega_b \times] (\tilde{I}_b \omega_b + \mathcal{W} h_w^W)] \right] \quad (32)$$

where \tilde{I}_b is an error coefficient representing the maximum possible error between an assumed inertia \tilde{I}_b and the true inertia I_b along the diagonals only (i.e. no products of inertia are considered). From (32), $F(x)$ indicates the function evaluated with values from the auxiliary controller and $F(x_d)$ indicates the function evaluated with values from the primary controller, i.e.:

$$F(x) = F(\tilde{x}(\tau)) \quad (33)$$

$$F(x_d) = F(z^*(\tau, v^*(\tau, z(t_k)))) , \tau \in [t_k, t_k + T] \quad (34)$$

6. Simulation and experimental results

6.1. Scenario description

A simulated rest-to-rest attitude tracking maneuver in the presence of external disturbances and reaction wheel faults is used to verify the proposed strategies. The maneuver is represented by a square wave on the Z -axis, alternating between pointing at 0° and 10° every 75s. This maneuver corresponds to a slew from $q_{1:3} = [0 \ 0 \ 0]$ to $q_{1:3} = [0 \ 0 \ -0.0872]$. Note in this paper we consider the restriction $q_4 \geq 0$, which results in the negative q_3 element. Simulations are implemented in MATLAB via direct multiple shooting with CasADi, which includes the nonlinear optimization library IPOPT [28]. System parameters, initial conditions, and gain values are provided in Table 1. All weighting matrices were user-defined and tuned manually. The value of the disturbance is randomized but satisfies an upper bound $W = \tau_{ext,max} = 3 \times 10^{-3}$ mN m. Fault affliction is also randomized. Three operating modes, indicated as $\sigma_j, j = 1 \dots 3$, are considered: Nominal, Fault 1, and Fault 2. Fault 1 is characterized by a float failure of a randomly selected wheel ($\alpha_i = 1$), while Fault 2 is characterized by a loss of efficiency failure ranging from $0.5 \leq \alpha_i \leq 0.95$ on another randomly selected wheel. The faults are compounding, such that Fault 2 includes the failure of Fault 1 when it is applied. Based on these values of α , the upper bound of the faults in the body frame is determined to be $\bar{\alpha} B_u = 11.4$ mNm. The state and input constraint sets are:

$$\mathcal{X} = \{-0.3536 \leq q_1 \leq 0.3536,$$

$$-0.1464 \leq q_2 \leq -6.852 \times 10^{-4},$$

$$-0.8536 \leq q_3 \leq 0.8536, 0.3536 \leq q_4 \leq 0.9966,$$

$$|\omega_b| \leq 0.5 \text{ rad/s}\}$$

$$\mathcal{U} = \{|u_x| \leq 8.16 \text{ mN m}, |u_y| \leq 8.16 \text{ mN m}, |u_z| \leq 11.5 \text{ mN m}\}$$

where the quaternion constraints represent a pointing constraint of $\pm[45^\circ \ 45^\circ \ 90^\circ]$. The additional constraints for FT-NMPC-MPSMC $_{\xi}$ are $\Xi = \{0 \leq \xi \leq 1\}$ and $Y = \{|v| \leq 0.05\}$. The simulation time is set to 3min and begins in the Nominal mode (σ_1). Fault 1 (σ_2) is injected at 1min followed by Fault 2 (σ_3) at 2min. The sampling time is set to $T_s = 0.6$ s, with a time horizon of $T = 12$ s. Controller performance is evaluated through the root mean squared errors (RMSE) of the system trajectory with respect to the nominal response for the vector portion of the quaternion and the root mean square (RMS) value of the control input along each body axis. Both RMSE and RMS are evaluated as an average over 50 repeated simulations.

6.2. Benchmark: MPSMC v. FT-MPSMC

To highlight the benefit of employing the fault tolerant auxiliary controller, system performance of FT-NMPC-MPSMC is compared to NMPC-MPSMC. Table 2 presents the resultant RMSE and RMS data, showing that the two controllers perform nearly identically regarding

Table 1
System Parameters.

Parameter	Simulation Value	Experimental Value
\hat{I}_b (kgm ²)	$\begin{bmatrix} 0.0196 & -0.0033 & -0.001 \\ -0.0033 & 0.0217 & 0.0009 \\ -0.0010 & 0.0009 & 0.0287 \end{bmatrix}$	
\tilde{I}_b (kgm ²)	$\begin{bmatrix} 0.0039 & 0 & 0 \\ 0 & 0.0043 & 0 \\ 0 & 0 & 0.0057 \end{bmatrix}$	$\begin{bmatrix} 0.0088 & 0 & 0 \\ 0 & 0.0098 & 0 \\ 0 & 0 & 0.0129 \end{bmatrix}$
q_0	$\begin{bmatrix} 0 & 0 & 0 & 1 \end{bmatrix}^T$	–
ω_0 (rad/s)	$\begin{bmatrix} 0 & 0 & 0 \end{bmatrix}^T$	
η	0.02	0.008
λ	0.75	
λ'	0.65	1.25
NMPC Parameters		
Q, P	$diag(0.03 \ 0.03 \ 0.5 \ 0.03 \ 0.5 \ 0.5 \ 0.5)$	
R	$0.1\mathbb{I}_3$	
MPSMC Parameters		
Q', P'	$0.9\mathbb{I}_3$	
R'	$0.1\mathbb{I}_3$	
FT-MPSMC Parameters		
ξ	$0.6\mathbb{I}_3$	$0.3\mathbb{I}_3$
R''	$0.1\mathbb{I}_3$	

Table 2
Simulation Results.

	Quaternion State RMSE		
	q_1	q_2	q_3
NMPC-MPSMC	0.00713	0.00544	0.00906
FT-NMPC-MPSMC	0.00710	0.00547	0.00911
FT-NMPC-MPSMC _{ξ}	0.00489	0.00388	0.00659
FT-NMPC-MPSMC _{ξ}	0.00466	0.00373	0.00632
	Control Torque RMS (mN m)		
	u_x	u_y	u_z
NMPC-MPSMC	0.0719	0.0758	0.170
FT-NMPC-MPSMC	0.0741	0.0758	0.172
FT-NMPC-MPSMC _{ξ}	0.0806	0.0828	0.196
FT-NMPC-MPSMC _{ξ}	0.0832	0.0853	0.202

tracking and control effort. The graphical data displayed in Fig. 2, illustrating the attitude response across the vector quaternion for each controller, confirms this. Both controllers maintain decent tracking until the introduction of the second fault where the system trajectories diverge from the nominal trajectory across the states. However, the graphical data also show the importance of the proposed design, most noticeably in state q_1 , where NMPC-MPSMC shows several tube violations as a result of the fault and the FT-NMPC-MPSMC shows none. Because it includes W_L instead of W in its formulation, the proposed control successfully encapsulates all system trajectories in its tube. This demonstrates that combining the maximum possible expected fault contribution with the maximum possible expected disturbance level maintains the RCI property of the NMPC-MPSMC’s tube, thus imbuing the controller with a fault tolerant quality in the presence of both forms of uncertainty.

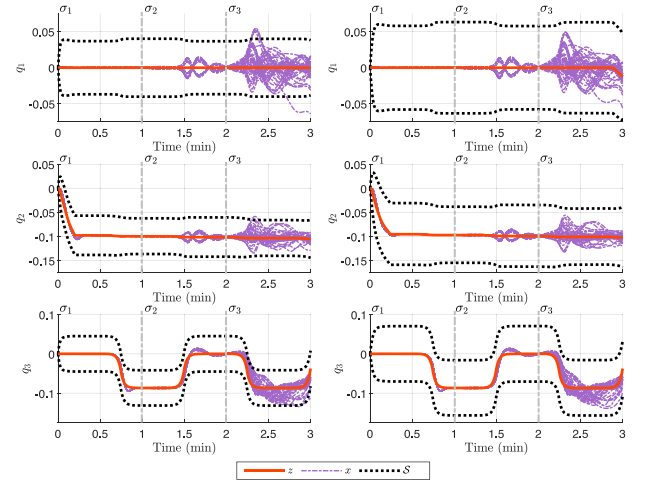


Fig. 2. System trajectories for NMPC-MPSMC (left) and FT-NMPC-MPSMC (right).

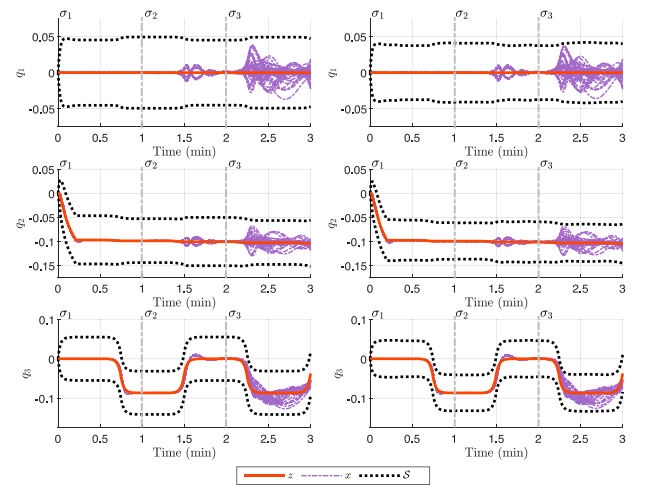


Fig. 3. System trajectories for FT-NMPC-MPSMC _{ξ} (left) and FT-NMPC-MPSMC _{ξ} (right).

6.3. FT-MPSMC expansions

In this section, the performance of the augmented forms of the FT-MPSMC are compared to investigate the effect of the double boundary layer and blended tube design. Fig. 3 illustrates identical trajectory trends to Fig. 2. As predicted, the spread of the trajectories is slightly narrower than FT-NMPC-MPSMC for both augmented controllers suggesting improved resilience to actuator faults. Further, both augmented controllers are able to maintain all trajectories in their tubes due to the addition of $\bar{\alpha}B_u$, again highlighting that RCI is maintained. Of special interest is that FT-NMPC-MPSMC _{ξ} appears to have about the same tube size across the vector quaternion as NMPC-MPSMC and yet is able to maintain all trajectories in the tube. Fig. 4 presents the tube size for q_1 and confirms this observation. Both augmented controllers’ tubes fall in the range between those of NMPC-MPSMC and FT-NMPC-MPSMC as expected due to the effect of ξ . The tube for FT-NMPC-MPSMC _{ξ} is closer to the disturbance-only based tubes due to $\xi = 0.6\mathbb{I}_3$, which also indicates that the tube formulation used more of the inner boundary layer. The impact of a dynamic ξ is clearly seen for FT-NMPC-MPSMC _{ξ} , where the tube remains close to that of NMPC-MPSMC but fluctuates with change in ξ allowing it to widen enough to maintain all system trajectories when appropriate.

The effect of the double boundary layer is best seen by the improved tracking performances of the augmented controllers presented in Table 2. Recall that FT-NMPC-MPSMC can be thought of as a version of the controller where $\xi = 0$ and no inner boundary layer is present. From

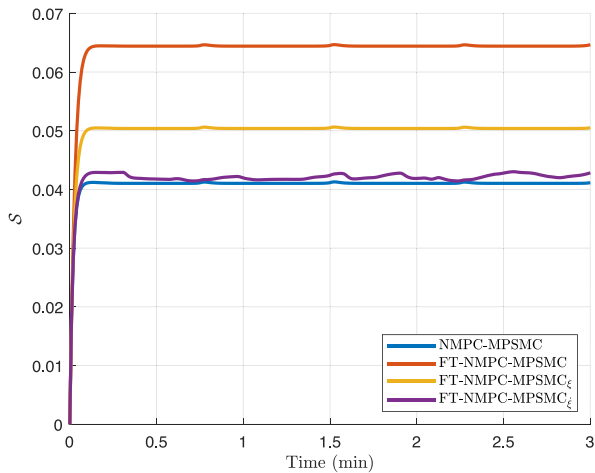


Fig. 4. Tube size across controllers for q_1 .

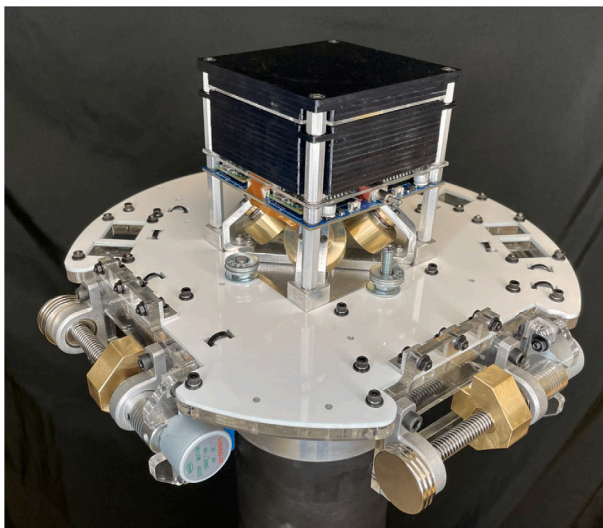


Fig. 5. The Nanosatellite Attitude Control Simulator (NACS) in the ICE lab at McMaster University.

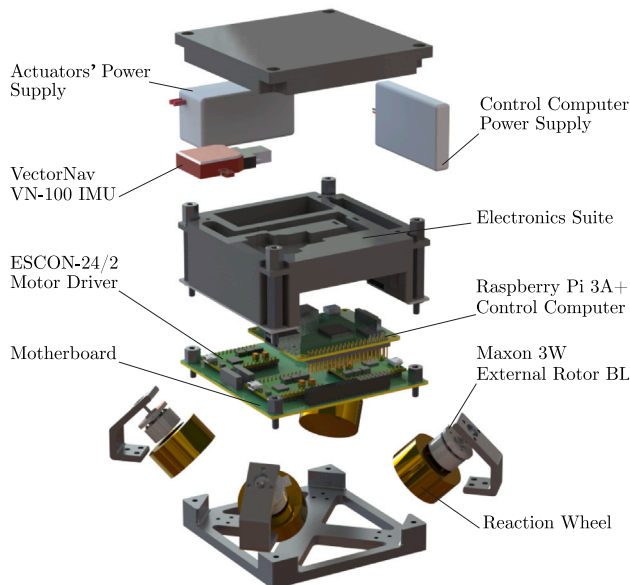


Fig. 6. MockSat exploded view and internal components [29].

Table 3
Comparison to SMC Results.

	Quaternion State RMSE		
	q_1	q_2	q_3
FT-SMC	0.00332	0.00281	0.0212
NMPC-MPSMC	0.00942	0.0983	0.0134
FT-NMPC-MPSMC	0.00921	0.0957	0.0134
FT-NMPC-MPSMC $_{\xi}$	0.00788	0.0957	0.0114
FT-NMPC-MPSMC $_{\xi}$	0.00776	0.0983	0.0112

this baseline, the inclusion of an inner boundary layer significantly reduces the RMSE. Indeed, both augmented controllers have pointedly lower RMSEs than both NMPC-MPSMC and FT-NMPC-MPSMC, with FT-NMPC-MPSMC $_{\xi}$ having the lowest, reflecting the observed reduction in trajectory spread from Fig. 2. Of note, however, is the increase in RMS for both augmentations. This is not surprising given that a typical tradeoff in sliding mode control is tracking accuracy versus control effort, where improved tracking results in increased control effort. However, the RMSE and RMS provided show that including ξ barely exacerbates this tradeoff, where tracking accuracies are reduced by a third and RMS increases at a maximum of around 0.03 mN m. This implies an advantage to including the double boundary layer formulation as the system benefitted from improved performance at little cost to applied torque.

6.4. Comparison to SMC

While the purpose of this paper is to explore tube-based control, this subsection briefly comments on the efficacy of implementing the tube-based controllers as opposed to implementing solely SMC. A fault tolerant SMC (FT-SMC) with saturated input was derived based on the SMC formulation of FT-NMPC-MPSMC and simulated on the system. New RMSE values, now based on the difference between the system trajectories and the reference rest-to-rest trajectory, are presented in Table 3 to compare performance. As seen, FT-SMC outperforms all tube-based controllers except in state q_3 . However, these results do not detract from the importance of the proposed method. Recall MPC-based techniques offer a range of benefits, including constraint adherence and information preview, that cannot be incorporated into well-established but simple controllers, such as SMC. Though not explored in this work, constraint violations can occur even in input saturated SMC [24]. Thus, despite the results in Table 3, the proposed schemes holistically have more to offer than the basic control scheme.

6.5. Experimental implementation

The proposed fault tolerant controllers were experimentally validated on the Nanosatellite Attitude Control Simulator (NACS) in the Intelligent and Cognitive Engineering (ICE) Laboratory at McMaster University. The simulator includes a Mock 1U CubeSat (MockSat), equipped with a redundantly configured reaction wheel array; an Automatic Balancing System (ABS), which attempts to align the Center of Mass (CM) with the Center of Rotation (CR); and a custom hemispherical air bearing, which provides a near-frictionless 3-DOF joint. The MockSat is equipped with a Raspberry Pi 3A+, inertial measurement unit (IMU), custom motherboard, two lithium polymer power supplies, and four reaction wheel actuators. The NACS is shown below in Fig. 5, and an exploded view of the MockSat is provided in Fig. 6.

Due to the MockSat's limited on-board computational resources, the proposed controllers are offloaded to a Desktop PC (Intel® Core™ i7-7700K CPU @ 4.20 GHz Processor) to allow for soft real-time implementation. Controllers are implemented in Python3.8 using CasADi. Information is exchanged between the Desktop PC and the on-board computer through a TCP Socket, in which serialization is achieved with Python's 'Pickle' package. The state vector is polled from the IMU once per control loop execution ($T_s = 0.6s$) and sent to the Desktop

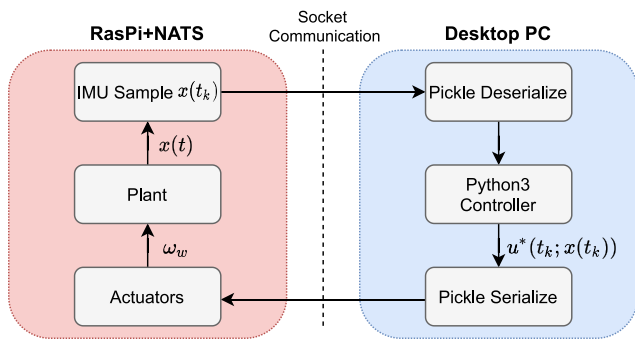


Fig. 7. Block diagram of the experimental procedure.

PC, after which the MockSat waits for a reply. Control body torques are calculated on the Desktop PC, decomposed into desired reaction wheel accelerations, and then passed back to the MockSat. Reaction wheel accelerations are passed to the motor controller in the form of various PWM signals. The block diagram shown in Fig. 7 illustrates the data passing between Desktop PC and MockSat. Further information regarding the NACS can be found in [29].

In the experiments, the MockSat performs a rest-to-rest attitude maneuver from an arbitrarily acquired initial attitude, to a 25° offset about the Z-axis from the initial position. The maneuver is performed in the presence of an extreme fault scenario, selected here to be characterized by $\alpha_1 = 1, \alpha_2 = 0.95, \alpha_3 = 0, \alpha_4 = 0$ indicating a majority failure with respect to the Y-axis. Additionally, the quaternion constraints are redefined to reflect the physical limitations of the testbed, resulting in new state constraints

$$\begin{aligned} \mathcal{X} = \{ & -0.1825 \leq q_1 \leq 0.1825, \\ & -0.1163 \leq q_2 \leq -5.50 \times 10^{-4}, \\ & -0.8234 \leq q_3 \leq 0.8234, \\ & 0.5246 \leq q_4 \leq 0.9977, \\ & |\omega_b| \leq 0.5 \text{ rad/s} \}, \end{aligned}$$

whereas input constraints remain unchanged. Finally, the upper bound of the disturbance is redefined to be $W = 0.0184$ mN m based on potential torque imbalances from the air bearing. All experimental parameters are defined in Table 1.

The numerical results displayed in Table 4 show that each controller has comparable tracking errors in q_1 and q_3 , but not q_2 , where the FT-NMPC-MPSMC $_{\bar{\chi}}$ performs best. This potentially suggests the controller compensates best for the failure across the Y-axis. Additionally, FT-NMPC-MPSMC exerts the most control effort, being significantly higher across the X-axis than its counterparts. The outcomes in Table 4 differ from the trend previously identified in Table 2. While the reasons for this difference require additional investigation, it is possible discrepancies in the simulated and experimental systems could have led to varied controller performance outcomes. This could include inability to accommodate all types of experimental disturbances in simulation or modeling differences (see Fig. 8).

7. Conclusions

This paper presented a novel approach for fault tolerant tube-based NMPC. The approach exploited a sliding mode formulation to incorporate faults as an additional form of disturbance, resulting in a disturbance upper bound able to account for external disturbances and actuator faults. To address potential overconservatism, the approach was extended to include a double boundary layer design which was examined as a static and dynamic variable. Simulation results on a nonlinear nanosatellite system illustrated the efficacy of the FT-NMPC-MPSMC schemes which maintained robust control invariance in the

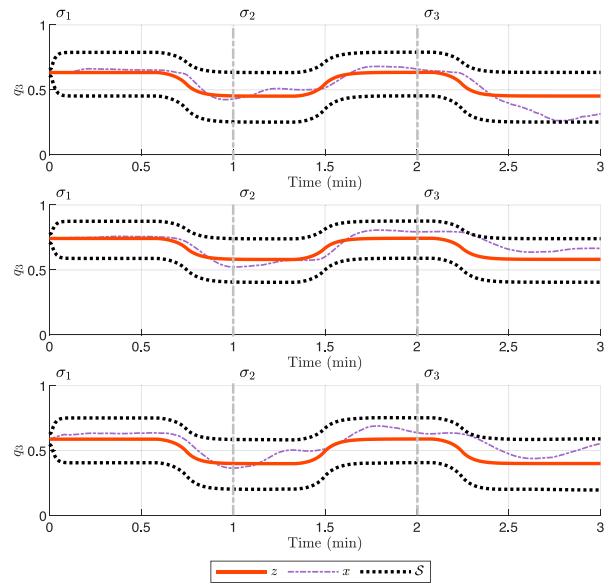


Fig. 8. Experimental system trajectory for q_3 per controller; from top: FT-NMPC-MPSMC, FT-NMPC-MPSMC $_{\bar{\chi}}$, FT-NMPC-MPSMC $_{\bar{\zeta}}$.

Table 4

Experimental Results.

	Quaternion State RMSE		
	q_1	q_2	q_3
FT-NMPC-MPSMC	0.00294	0.00759	0.0733
FT-NMPC-MPSMC $_{\bar{\chi}}$	0.00313	0.00447	0.0818
FT-NMPC-MPSMC $_{\bar{\zeta}}$	0.00328	0.00169	0.0882
	Control Torque RMS		
	u_x (mN m)	u_y (mN m)	u_z (mN m)
FT-NMPC-MPSMC	0.342	0.350	0.539
FT-NMPC-MPSMC $_{\bar{\chi}}$	0.0896	0.112	0.283
FT-NMPC-MPSMC $_{\bar{\zeta}}$	0.0957	0.0924	0.356

face of disturbances and faults. The addition of the double boundary layer minimized trajectory spread and improved tracking performances with minimal increases in control effort. Further, the proposed techniques were successfully validated experimentally on the NACS. Future work includes investigation of more complex fault modes, expansion to active FTC, and implementation on additional testbeds.

CRedit authorship contribution statement

Elyse Hill: Conceptualization, Methodology, Software, Investigation, Writing – original draft. **Andrew Newton:** Methodology, Software, Investigation, Experimentation, Writing – original draft. **S. Andrew Gadsden:** Conceptualization, Investigation, Writing – review & editing, Supervision, Project administration, Funding acquisition. **Mohammad Biglarbegian:** Conceptualization, Investigation, Writing – review & editing, Supervision, Project administration, Funding acquisition.

Declaration of competing interest

The authors declare that they have no known competing financial interests or personal relationships that could have appeared to influence the work reported in this paper.

Data availability

Data will be made available on request.

Acknowledgments

We would like to acknowledge funding from the Natural Science and Engineering Research Council of Canada (Discovery Grant: Gadsden and Biglarbegian).

References

- [1] Zhang Y, Jiang J. Bibliographical review on reconfigurable fault-tolerant control systems. *Annu Rev Control* 2008;32(2):229–52.
- [2] Jiang J, Yu X. Fault-tolerant control systems: A comparative study between active and passive approaches. *Annu Rev Control* 2012;36(1):60–72.
- [3] Essers M, Vaneker T. Design of a decentralized modular architecture for flexible and extensible production systems. *Mechatronics* 2016;34:160–9, System-Integrated Intelligence: New Challenges for Product and Production Engineering.
- [4] Hernandez-Alcantara D, Amezquita-Brooks L, Morales-Menendez R, Sename O, Dugard L. The cross-coupling of lateral-longitudinal vehicle dynamics: Towards decentralized fault-tolerant control schemes. *Mechatronics* 2018;50:377–93.
- [5] Jayasenthil R, Choi S. A novel semi-active control strategy based on the quantitative feedback theory for a vehicle suspension system with magneto-rheological damper saturation. *Mechatronics* 2018;54:36–51.
- [6] Chung W, Son H. Fault-tolerant control of multirotor UAVs by control variable elimination. *IEEE/ASME Trans Mechatronics* 2020;25(5):2513–22.
- [7] Jiang K, Kheradmandi M, Hu C, Pal S, Yan F. Data-driven fault tolerant predictive control for temperature regulation in data center with rack-based cooling architecture. *Mechatronics* 2021;79:102633.
- [8] Ma Y, Jiang B, Cocquemot V. Modeling and adaptive fault compensation for two physically linked 2wd mobile robots. *IEEE/ASME Trans Mechatronics* 2021;26(2):1161–71.
- [9] Wang J, Pan H, Sun W. Event-triggered adaptive fault-tolerant control for unknown nonlinear systems with applications to linear motor. *IEEE/ASME Trans Mechatronics* 2021;1.
- [10] Huang C, Naghdy F, Du H. Delta operator-based fault estimation and fault-tolerant model predictive control for steer-by-wire systems. *IEEE Trans Control Syst Technol* 2018;26(5):1810–7.
- [11] Hill E, Gadsden SA, Biglarbegian M. Explicit nonlinear MPC for fault tolerance using interacting multiple models. *IEEE Trans Aerosp Electron Syst* 2021;57(5):2784–94. <http://dx.doi.org/10.1109/TAES.2021.3065089>.
- [12] Knudsen BR, Alessandretti A, Jones CN, Foss B. A nonlinear model predictive control scheme for sensor fault tolerance in observation processes. *Internat J Robust Nonlinear Control* 2020;30(14):5657–77.
- [13] Raimondo DM, Marseglia GR, Braatz RD, Scott JK. Fault-tolerant model predictive control with active fault isolation. In: Conference on control and fault-tolerant systems. Nice, France: IEEE; 2013, p. 444–9.
- [14] Raimondo DM, Boem F, Gallo A, Parisini T. A decentralized fault-tolerant control scheme based on active fault diagnosis. In: Proc. 55th conference on decision and control. Las Vegas, NV: IEEE; 2016, p. 2164–9.
- [15] Ben Chabane S, Maniu CS, Camacho EF, Alamo T, Dumur D. Fault tolerant control approach based on multiple models and set-membership state estimation. In: Proc. European control conference. Aalborg, Denmark: IEEE; 2016, p. 1105–10.
- [16] Xu F, Puig V, Ocampo-Martinez C, Oлару S, Niculescu SI. Robust MPC for actuator-fault tolerance using set-based passive fault detection and active fault isolation. *Int J Appl Math Comput Sci* 2017;27(1):43–61.
- [17] Huang C, Naghdy F, Du H. Observer-based fault-tolerant controller for uncertain steer-by-wire systems using the delta operator. *IEEE/ASME Trans Mechatronics* 2018;23(6):2587–98.
- [18] McCloy R, De Doná J, Seron M. Fault-tolerant fusion-based MPC with sensor recovery for constrained LPV systems. *Internat J Robust Nonlinear Control* 2018;28(11):3589–605.
- [19] Boem F, Gallo AJ, Raimondo DM, Parisini T. Distributed fault-tolerant control of large-scale systems: An active fault diagnosis approach. *IEEE Trans Control Netw Syst* 2020;7(1):288–301.
- [20] Zhang R, Wu S, Cao Z, Lu J, Gao F. A systematic min–max optimization design of constrained model predictive tracking control for industrial processes against uncertainty. *IEEE Trans Control Syst Technol* 2018;26(6):2157–64.
- [21] Shi H, Li P, Su C, Wang Y, Yu J, Cao J. Robust constrained model predictive fault-tolerant control for industrial processes with partial actuator failures and interval time-varying delays. *J Process Control* 2019;75:187–203.
- [22] Khan O, Mustafa G, Khan AQ, Abid M, Ali M. Fault-tolerant robust model-predictive control of uncertain time-delay systems subject to disturbances. *IEEE Trans Ind Electron* 2021;68(11):11400–8.
- [23] Paulson JA, Heirung TAN, Mesbah A. Fault-tolerant tube-based robust nonlinear model predictive control. In: Proc. American control conference. Philadelphia, PA; 2019, p. 1648–54.
- [24] Hill E, Gadsden SA, Biglarbegian M. Robust nonlinear model predictive control with model predictive sliding mode for continuous-time systems. *J Dyn Syst Meas Control* 2021;144(3):031006.
- [25] Magni L, Raimondo D, Allgower F, editors. *Nonlinear model predictive control: Towards new challenging applications*. In: Lecture notes in control and information sciences, vol. 386, Chennai, India: Springer-Verlag; 2009, p. 1–26.
- [26] Rawlings JB, Mayne DQ, Diehl M. *Model predictive control: Theory, computation, and design*. 2nd ed.. Santa Barbara: Nob Hill Publishing; 2017.
- [27] Findeisen R, Raff T, Allgöwer F. *Sampled-data nonlinear model predictive control for constrained continuous time systems*. *Lecture Notes in Control and Inform Sci* 2007;346:207–35.
- [28] Andersson JAE, Gillis J, Horn G, Rawlings JB, Diehl M. CasADi – A software framework for nonlinear optimization and optimal control. *Math Program Comput* 2019;11(1):1–36.
- [29] Newton A. *Design, development, and experimental validation of a nanosatellite attitude control simulator*. [Masters thesis], Guelph, Ontario: Univ. of Guelph; 2021.



Elyse Hill received a Bachelors of Science in Mechanical Engineering from the University of Maryland, Baltimore County (USA). She then completed her PhD in Mechanical Engineering at the University of Guelph (Ontario, Canada) in the area of control theory. Elyse is currently a NASA Postdoctoral Research Fellow at the Glenn Research Lab in Cleveland, Ohio, USA. Her research interests include model predictive control, fault tolerant control, and nonlinear systems, with a focus on aerospace applications.



Andrew Newton received his Bachelor of Mechanical Engineering, with Distinction, from the University of Guelph. He continued at Guelph to complete his MASC (Engineering), where he designed, fabricated, and programmed a nanosatellite attitude control simulator. He is currently a Research Engineer in the Department of Mechanical Engineering at McMaster University, where he is developing an aircraft-mounted robotic control system for NASA's air-LUSI instrument. His research interests include robotics, computer vision, nonlinear controls, and state estimation, with a particular interest in aerospace applications.



S. Andrew Gadsden earned his Bachelors in Mechanical Engineering and Management (Business) at McMaster University. He then completed his PhD in Mechanical Engineering at McMaster in the area of estimation theory and mechatronics. Andrew worked as a postdoctoral researcher at the Centre for Mechatronics and Hybrid Technology (Ontario, Canada), and also worked concurrently as a Project Manager in the pharmaceutical industry (Apotex Inc, Toronto, Ontario). Andrew is an Associate Professor in Mechanical Engineering at McMaster University with a research focus in control and estimation theory, and applied artificial intelligence and machine learning. Before joining McMaster University, he was an Associate/Assistant Professor at the University of Guelph and an Assistant Professor in the Department of Mechanical Engineering at the University of Maryland, Baltimore County (USA). Andrew works/worked with a number of colleagues in NASA, the US Army Research Laboratory (ARL), US Department of Agriculture (USDA), National Institute of Standards and Technology (NIST), and the Maryland Department of the Environment (MDE). He is an elected Fellow of ASME, is a Senior Member of IEEE, and is a Professional Engineer of Ontario. Andrew is also a reviewer for a number of ASME and IEEE journals and international conferences.



Mohammad Biglarbegian received his BSc degree (Hons.) from the University of Tehran in Tehran, Iran. He earned his MASC from the University of Toronto (Ontario, Canada) and his PhD from the University of Waterloo (Ontario, Canada). He is currently an Associate Professor with the Department of Mechanical and Aerospace Engineering at Carleton University (Ottawa, Ontario) and is the Director of the Autonomous and Intelligent Control for Vehicles (AICV) Research Laboratory. Prior to Carleton, he was an Associate and Assistant Professor in the School of Engineering at the University of Guelph. His research interests include advanced control, robotics, estimation, and optimization for different mechatronics systems; particularly advanced autonomous robotics and vehicles. Mohammad received the University of Guelph Research Excellence Award in 2018. He currently serves as the associate editors for two international journals of Robotics and Automation as well as Intelligence and Robotics.